ACS APPLIED POLYMER MATERIALS

pubs.acs.org/acsapm Article

Microscopic Hybrid Membranes Made of Cellulose-Based Materials Tuned for Removing Metal Ions from Industrial Effluents

Zoheb Karim* and Susanna Monti*

Cite This: https://doi.org/10.1021/acsapm.1c00105 Read Online

ACCESS | Metrics & More | Article Recommendations | Supporting Information

ABSTRACT: Most of the polymeric membranes used today in water decentralization are synthesized through complicated and expensive processes, contain unrenewable petrochemical building blocks, and are characterized by untailored surfaces. Besides their significant drawbacks, they do not comply with environmental requirements and regulations and thus should be replaced with more eco-friendly products. The urgent need is to create robust and tunable nano/micro materials for confidently designing efficient and selective polymeric water filters with guaranteed sustainability and biodegradability. Active hybrid membranes made of eco-friendly high-grade microfibrillated cellulose (MFC), appropriately functionalized, have shown superior performance during the separation of metal ions from the industrial effluents, and their separation efficiency has been found to be tunable with a proper selection of type and density of the functional groups. On the basis of these findings and needs, we have developed a chemo-enzymatic functionalization strategy for grafting methyl and phosphate groups on the MFC fibers. This methodology can calibrate the interlayer fiber spacing and control the pore-size distribution of the membranes appropriately. We demonstrate this in the present work by characterizing the impact of Mg^{2+} and Cr^{3+} ions and their mixture (Mg^{2+} and Cr^{3+}) on the membrane separation performance extensively by using various experimental techniques and computational methods. Moreover, we have adapted this sustainable, fully water-based system for upscaling the hybrid membranes in continuous mode by resorting to the phosphate-MFC membranes for the spiral-bound modules in cartridge use. We have developed the flow-through (FTM) and flow-over (FOM) modules and tested them to separate metal ions from the industrial effluent, ensuring regeneration and reusability. Our results indicate that these prototype hybrid MFC membranes represent the most promising type of next-generation high-performance filtration devices for a more sustainable society.

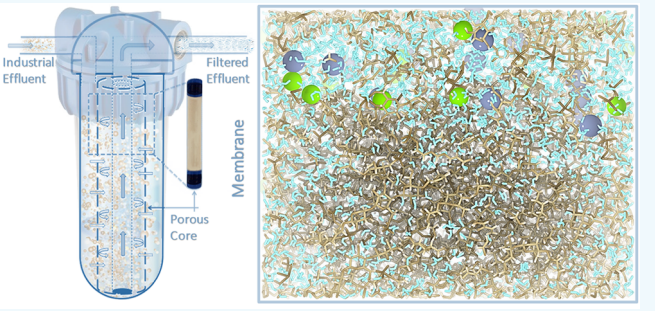

KEYWORDS: *sustainability, spiral wound modules, microfibrillated cellulose, modified surface, functionalization*

INTRODUCTION

The increasing population growth, urbanization, and rapid industrialization are continually putting pressure on the global water demand, which is translated into an alarming scenario where available freshwater supply is no longer matching the patterns of the running developments.[1−5] Pressure-derived membrane separation has long served as a feasible option to provide safe water in many deserted areas, coastal regions, or remote.[6−8] Despite its versatility in tackling water scarcity, this type of membrane has been unfavorably addressed as the most energy-intensive water treatment technology with high costs and energy demand.[9,10] These combined requirements are often beyond the impoverished communities' possibilities that desperately need low-cost, safe drinking water. Furthermore, most polymeric membranes for water filtration (microfiltration to ultrafiltration), including hollow fibers and spiral wound, are manufactured by the phase inversion method[7,8,11] that produces structures with intrinsic limitations, like low water flux (high energy cost), high fouling tendency, and an asymmetric pore morphology across the membrane thickness.[12−14]

Under the framework of the European Union (EU) green circular economy, biobased polymers for water filtration are being promoted as an alternative to petrochemical-based polymers for preserving and improving the environment for the future. Consumers are also more attracted by these eco-friendly products that can either replace or, at least, reduce the dependence on petrochemicals.[15]

In this context, nanocellulose, prepared through a top-down approach from wood biomass and, in particular, microfibrillated cellulose (MFC), has shown high efficiency for the removal of

Received: January 23, 2021
Accepted: June 17, 2021

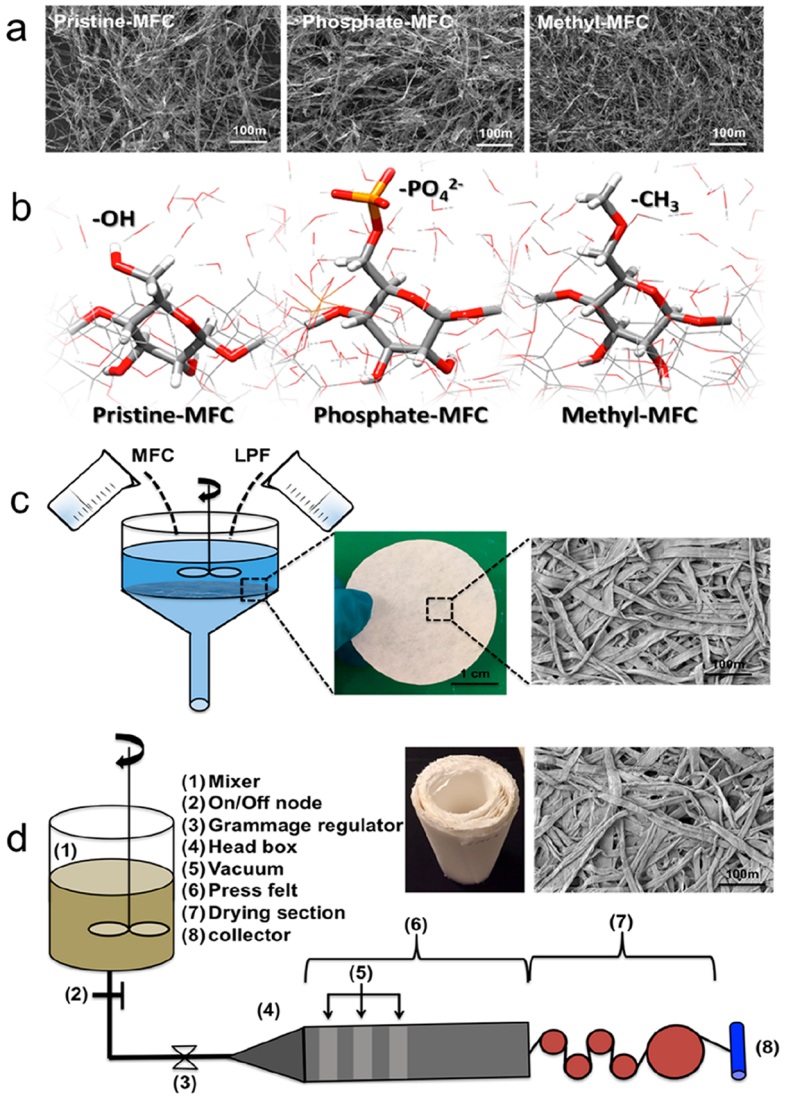

Figure 1. Summary of functional groups grafted on the surface of microfibrillated cellulose (MFC). (a) SEM images of functionalized MFC were captured after freeze-drying. Computational 3D structures of the three functional groups (hydroxyl-, phosphate-, and methyl-) (b). Lab-scale fabrication of composite membranes using pristine and functionalized MFC. The hybrid approach was followed to maintain a highly porous structure. (c) Thus, long pine fibers (LPFs) were mixed with MFC for the fabrication of membranes using vacuum-filtration. The image also shows the produced composite membranes and the SEM image at low resolution. (d) Scaling up of composite membranes for the production of spiral wound modules was performed using the traditional paper making approach. The Experimental Paper Machine (XPM) was used for the production of composite membranes via the roll-to-roll method in continuous mode (Figure S1).

various pollutants and has been modified and improved for this action extensively by several groups.[16−18] Indeed, MFC has unique characteristic properties, including high aspect ratio (>100), crystallinity (65−95%), tensile strength (200−300 MPa), elastic modulus (6−7 GPa), and low ζ-potential (−10 mV).[3,19] Furthermore, the MFC adsorption ability and its tendency to form stable networks when dried make it an excellent candidate for flat sheet membranes or module processing. As demonstrated by our group in earlier works,[20−23] MFC could be a useful, functional, and robust biobased material in the field of water purification.

The removal of charged impurities by adsorption on MFC membranes functionalized with charged moieties[17,18] has the advantage of lowering both the pressure and energy demands without compromising the membrane selectivity. Even though this area is a hot topic, only very few studies on the separation of the charged impurities via affinity membranes with nano/microfiber technology have been reported in the literature.[16,24,25]

Furthermore, extending the scale from the lab prototypes (centimeter size) to the industrial pilot systems without compromising water flux, selectively, mechanical stability, and pore-size distribution is a huge design challenge. We have faced this issue using the traditional paper-making approach through the Experimental Paper Machine (XPM) and introduced pulp fibers (5−25 μm diameter) as a matrix during the preparation process for improving the porosity of the pristine MFC membranes. These fibers have a more open networking potential[3,26,27] and determine an ultrafast water flow in the microfiltration range. We selected the commercial-grade MFC with a high charge density and characterized it with a great variety of experimental techniques and computational studies at the atomic level. These simulations were very useful to disclose the various types of supramolecular structures and the

https://doi.org/10.1021/acsapm.1c00105
ACS Appl. Polym. Mater. XXXX, XXX, XXX−XXX

interactions of the grafted active groups (i.e., phosphate (PO_3^{2-}), methyl (CH_3), carboxylic ($-COO^-$), hydroxyl ($-OH$)) with the metal ions. Our final result is the development of a fully biobased high-performance, functionally active MFC-based membranes system that is entirely sustainable, biodegradable, and reusable.

We employed the chemo-enzymatic functionalization (i.e., phosphorylation using enzyme hexokinase and chemical catalysis) to increase the density of the selected functional groups for the effective separation of the pollutants and technology transfer via a scaling up of active hybrid membranes, which was utilized in continuous mode. To demonstrate the idea, we designed and developed spiral wound modules that were used as a cartridge for the separation of the metal ions from the industrial effluent. Interactive nanoscale analysis of the grafted functional groups in the presence of the impurities was performed using various sophisticated techniques flanked by classical molecular dynamics simulations based on a reactive force field. These could describe bond breaking and formations and all the interactions between the model MFC matrixes and the polluted solution efficiently, providing a reliable interpretation of the experimental finding and predictions of the effects deriving from the materials modulations. Likewise, these fabricated fully biobased sustainable composite membranes have the capability to emerge as new generation composite membranes for the separation of charged nanopollutants like metal ions and could be used in the future for dyes, drugs, bacterias, viruses, etc. These functionalized microfiltration composite membranes can be upscaled in a complete water-based-system (continuous mode). Furthermore, an effective design of the spiral module could extend its removal capabilities to other pollutants present in solution. Thus, a new prototype of modules that is capable of being used at pilot/industrial scale for the continuous removal of pollutants from industrial effluent in the long-run has been reported here.

MATERIALS AND METHODS

High-grade microfibrillated cellulose (MFC) was provided for free by Borregaard AB, Sarpsborg, Norway. The charge density was close to 28.54 ± 4.09 μmol/g, and the dry concentration was 9.3 wt %.[28] Enzyme hexokinase was purchase from Novozymes, and all other chemicals used in this study were purchased from Sigma-Aldrich. All the chemicals (analytical grade) were used without any further purification. The industrial effluent (biosludge) contaminated with metal ions was collected from a cellulose production mill (paper and pulp industry) located in Sweden. Commercially available filters (cartridges), porous spacers, and impermeable barriers were purchased from IKEA.

Functionalization and Fabrication of MFC-Based Hybrid Active Membranes. First, pine fibers were wet up overnight for swelling and then disintegrated for 20 min (SR value 13.6). The fiber suspension was stored at 4 °C for further use as required. The grafting of functionally active polar and nonpolar groups (phosphate- and methyl-) was performed as mentioned in the Supporting Information, and the obtained charge density was 120.4 ± 1.2 and 8.6 ± 1.4 μmol/g for phosphate and methyl groups, respectively (Table S1).

Active hybrid membranes were fabricated using vacuum-filtration (Figure 1c), as described in a previous publication[3] (see details in the Supporting Information(SI)).

Upscaling and Module Design. Only phosphate-MFC functional composite membranes were upscaled. The composition of the scaled composite membranes was the same as the vacuum-filtered membranes (1:1 ratio, total 1 wt %). A traditional paper-making approach (Figure 1d) on Experimental Paper Machine (XPM) was used in continuous mode (Figure S1). The detailed process is reported in the Supporting Information and in a previous paper of ours.[27]

Modules of phosphate-MFC-based active composite membranes were produced as flow-through (FTM) and flow-over (FOM) designs (Figures S2 and S3).

Characterization of Grafted Functional Groups and Active Hybrid Membranes. The quantitative analysis of the functional groups was performed via titration.[3,28] The surface ζ-potential of the suspensions was measured using a Mutek SZP 06, MUTEK instrument (SI).

All functionally active hybrid membranes were characterized using an IR instrument (Varian 670-IR FTIR spectrometer) equipped with an attenuated total reflection (ATR) detector. All samples were scanned from 500 to 4000 cm^{-1}. The ^{13}C CP/MAS spectra were captured using 295 ± 1 K in a Bruker Avance III AQS 400 SB instrument operating at 9.4 T for pristine and methyl-CMF, and ^{31}P MAS NMR spectra were recorded in a Bruker Avance instrument using a MAS rate of 10 kHz and a 4 mm probe as reported previously.[3] The X-ray diffraction measurements were performed on a D/max III X-ray diffractometer (Rigaku Tokyo, Japan), equipped with nickel-filtered Cu Kα radiation (λ = 0.15418). Interlaminated spacing, d spacing was calculated using Bragg law,[29] for wet composite membranes first. Then the network was arrested through freeze-drying (Supporting Information). Furthermore, the surface wettability test was carried out by means of an optical contact angle meter at room temperature, with the sessile drop technique.[3] The particle size distribution of filtered polyethylene glycol (PEG) was characterized by laser diffraction (Mastersizer 3000, Malvern, UK). Mechanical properties of dry and wet modules were measured with a tensile tester (Lorentzen & Wettre, ABB), and strain stress cured was drawn using raw data.

Nano-/Microstructured Morphology and Pore-Size Distributions. The morphologies of MFC and fabricated active hybrid laminated membranes were analyzed using a scanning electron microscope (JEOL, JSM-6010LV, SEM). Furthermore, the high-resolution images of the active membranes were taken through a TESCAN MAIA3 Triglav (Supporting Information). The N_2 adsorption analysis was performed using a Micromeritics ASAP 2000 instrument for the measurement of the pore-size distribution.

Water Permeability of Active Hybrid Membranes and Modules. The water permeability of all vacuum-filtered hybrid membranes was analyzed through a customized dead-end cell apparatus (Figure S4a) as reported by Zhu et al.[16] In particular, an active filtration area of 90 cm^2 was considered for the water permeability measurement with a differential applied pressure of 0.5 bar. The water permeability of the spiral modules (flow-through module and flow-over module) was measured using a continuous flow system, as shown in Figure S4b. Differential pressures of 1−4 bar were applied for the constant water flow. It should be noted that only distilled water was employed for the active hybrid membranes except for the spiral modules, where distilled water and industrial effluent were used. For the continuous water filtration test with time, a Convergence clean water flux (CWF) pilot system was used as reported in a previous publication of ours.[3]

Separation of Metal Ions from Industrial Effluent. The industrial effluent contaminated with various metal ions (Table S2) was used to measure the efficiency of the vacuum-filtered hybrid membrane and the designed modules. The separation of metal ions (vol. 300 mL) through lab-based hybrid membranes was carried out with a customized dead-end-cell apparatus. For the spiral modules, 7 L of industrial effluent was passed through (FTM) or over (FOM) in a continuous process (Figure S4b). Quantitative and qualitative analyses of the metal ions after adsorption were recorded on an inductively coupled plasma optical emission spectrometer (ICP-OES) (details in the Supporting Information).

Representative Molecular Models and Molecular Dynamics Simulations. Possible models of the hybrid membranes functionalized with phosphates and methyl groups were built starting from an already optimized fiber that consisted of aligned glucosyl chains organized in a rod-like structure.[3,16−18] The original prototype was modified by adding, randomly, phosphate or methyl groups on the four long sides of the rod, in a concentration that agreed with the experiments (Figures S5 and S6). Then, to obtain the hybrid MFC matrixes, three fibers were combined, in each case (i.e., phosphate- or methyl-MFC models),

https://doi.org/10.1021/acsapm.1c00105
ACS Appl. Polym. Mater. XXXX, XXX, XXX−XXX

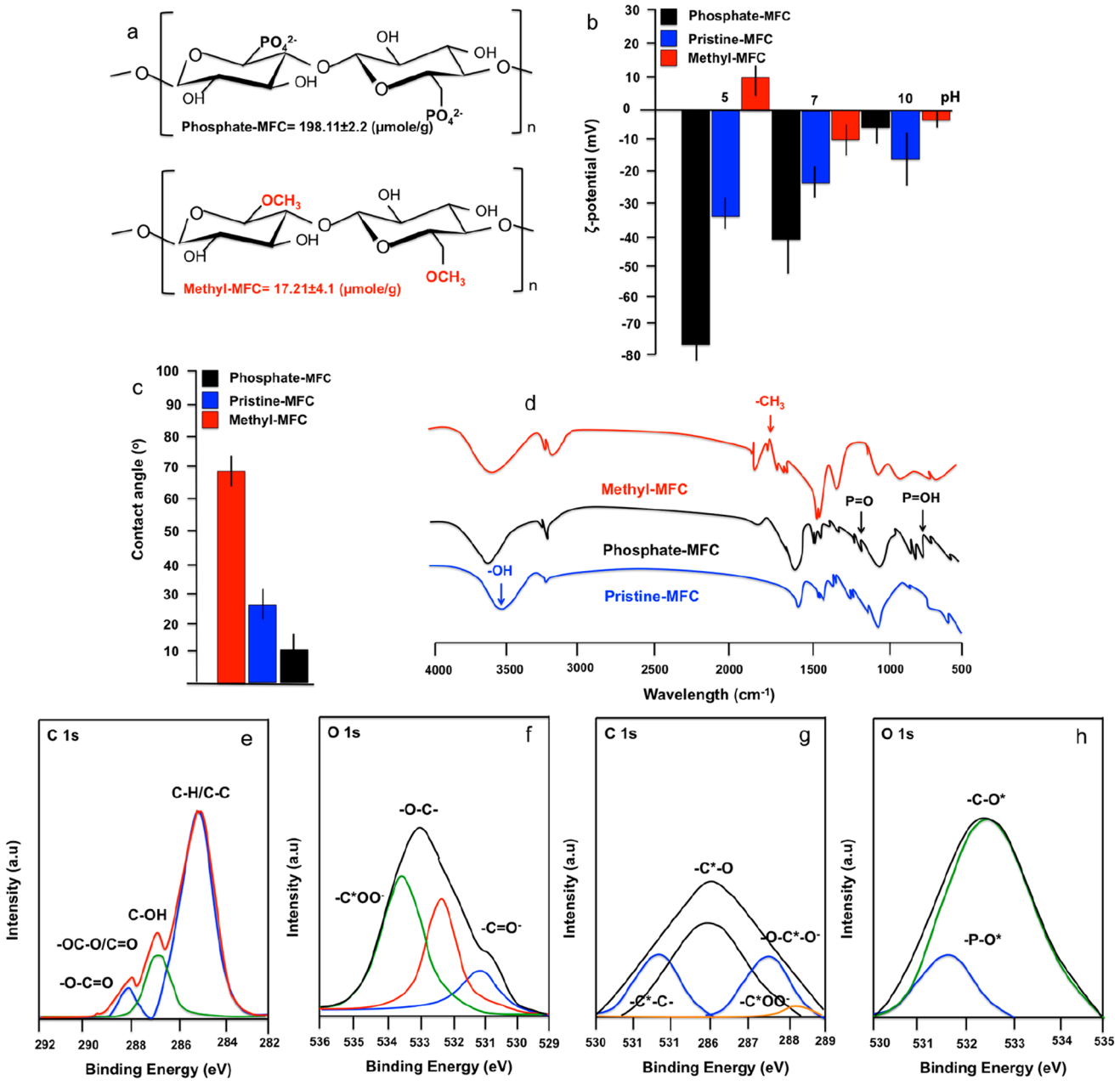

Figure 2. Characterization of grafted MFC using various advanced techniques. (a) Grafting of the phosphate (PO_4^{2-}) and the methyl ($-CH_3$) functional groups. (b) ζ-potential of pristine and modified MFC was calculated using a zeta-sizer. (c) Contact angle measurement was performed as reported in the text, and a very high contact angle was found for the nonpolar methyl grafted functional group. Grafted functional groups were further characterized using (d) FTIR and (e−h) XPS.

piling them one on top of the other (in the *Z*-direction) at an angle of approximately 60°. A packed disordered bulk representation of the hybrid cellulose-based filters (methyl-MFC and phosphate-MFC) was obtained by employing a series of molecular dynamics simulations in the NPT ensemble at ambient temperature and different pressures (Figure S7). This stage was mandatory to induce a compact reorganization of the chains in stable relative arrangements. Indeed, during the dynamics runs, the glucosyl chains changed their conformation and moved to other locations to produce more realistic packing densities of approximately 1.5 g/cm^3 (with a final box size of approximately 71 × 73 × 25 Å^3).

The last sampled geometries of the NPT production dynamics (final simulation at ambient temperature and pressure) were used as the starting arrangements of the simulations in solution. The phosphate- and methyl-MFC structures were solvated by adding water molecules and metal ions (40 ions and approximately 3000 water molecules) on top of one of their sides (plane XY), and periodic boundary conditions were applied in all directions to mimic an infinite system. Mg^{2+} and Cr^{3+} metal ions were randomly inserted in the added water layers, separately and in a 50−50% combination at a concentration that was defined on the basis of the experimental evidence. The analysis of the simulation results was focused on the last portion of the trajectories (100 configurations), considering atom−atom radial distribution functions (RDFs), percentage of surrounding species (within a 3.5 Å range), membrane pores, and tunnels. A visual examination of the final configurations was crucial to reveal possible adsorption trends in the two MFC architectures and connections with experiments. Here, it is worth mentioning that, under the influence of the surrounding solvent molecules, at the end of the production runs, the cellulose chain packing in each case became less compact and slightly inflated. Larger deviations

https://doi.org/10.1021/acsapm.1c00105
ACS Appl. Polym. Mater. XXXX, XXX, XXX−XXX

were found in the case of the phosphate functionalization that presented wider pockets and a more significant number of tunnels (Figure S8). For more details, see the Supporting Information.

RESULTS AND DISCUSSION

A first comparison between the functionalized MFC (-phosphate and -methyl) membranes and the pristine reference revealed that the first ones have a higher charged density (Table S1), which is more marked in the case of the phosphate functionalization. Instead, the SEM images displayed in Figure 1a, which depict the morphology of these materials, suggest that the differences are not significant (Figure 1b), and only a slight thickening of the fibers takes place after methylation. This seems to indicate more compact supramolecular arrangements. A parallel with the models obtained through molecular dynamics simulations revealed that the hydrophobic interactions of the methyl groups were responsible for the creation of the tightly packed structures with less porous glucosyl networks.[30,31]

Considering the scalable route, vacuum-filtration (Figure 1c), and the physical properties of the produced hybrids reported in Table S1, it was found a significant decrease in tensile strength after grafting both phosphate and methyl groups and the formation of porous materials with similar patterns in terms of densities and air permeance (Table S1). The diagrammatic representation of the hybrid membranes scaling up shown in Figure 1d together with the XPM details of Figure S1 indicates that there is no apparent significant difference between the vacuum-filtered and upscaled hybrid membranes (Figure 1c,d) except for high tensile strength in the case of the upscaled hybrids that could be due to the alignment of the long pine fibers toward the machine direction.[3,28,32−35]

The characterization of functionally active hybrid membranes was performed using various advanced techniques (Figure 2). The diagrammatic representation of the grafted functional groups on the surface of MFC is illustrated in Figure 2a (C6 position of cellulosic monomer). A highly negative surface ζ-potential was obtained for the phosphate-MFC membranes at acidic pH (Figure 2b), whereas a positive ζ-potential was recorded for the methyl-MFC membranes at acidic pH, and a decrease in the surface ζ-potential from acidic to alkaline took place in agreement with previous data.[36−38] The surface wettability was evaluated through contact angle measurements. A very high contact angle (68°) was recorded for the methylated system, and a decrease in the contact angle was observed for pristine- and phosphate-MFC-based membranes (Figure 2c). Again, it could be speculated that the contact angle increases with the hydrophobic nature of grafted moieties, in perfect agreement with the decrease in the polarity of grafted functional groups.[39]

The comparison of the attenuated total reflectance-Fourier transform infrared (ATR-FTIR) spectra of the grafted hybrid membranes with pristine reference identified changes in the structure through the appearance of the 1210 and 930 cm^{-1} signals in the case of the phosphorylation that could be assigned to the P═O and P—OH vibration modes, respectively,[40] and a decrease in the intensity and change in the profile for 3400 cm^{-1} band, which could be ascribed to the stretching of the O—H bond due to partial substitution of hydrogen groups during the methylation of MFC. Furthermore, an increase was observed for the band around 3200 cm^{-1} assigned to the C—H stretching due to the CH and CH_2 groups of cellulose and CH_3 of methyl-MFC (Figure 2d).[41]

A detailed X-ray photoelectron spectroscopy (XPS) analysis of modified MFCs is illustrated in Figure 2e−h. As expected, the spectra of the functionalized MFC showed signals from carbon (C 1s) and oxygen (O 1s) mainly. For methyl-MFC, the C 1s spectrum revealed the presence of different chemical bonds: C—H and C—C bonds at a binding energy of 284.4, a C—O bond at 286.3, one peak at 287.8 assigned to C—O and O—C—O bonds, and O—C—OR bonds at 290.5 eV.[42,43] High-resolution C 1s XPS spectra of phosphate-MFC are displayed in Figure 2g. The deconvolution into three subpeaks indicates three types of C—O bonds. The pristine-MFC had peaks at 284.4 (shoulder), 286.2 (strong), and 287.4 (shoulder) for C—C—, C—O, and —O—C—O—, respectively.[3,44] When phosphorylation occurs, the intensity of the peaks is significantly decreased due to the high amount of Mg ions.[40] Furthermore, a symmetrical strong O 1s peak at around 532.7 for —C—O, which changes to asymmetrical after phosphorylation, is shown in Figure 2h. The main O 1s peaks are still located at around 532.7 eV for —C—O, but a weak shoulder appears at around 531.5 eV for —P—O—.[3,45] A full XPS scan of the functionalized MFCs is given in Figure S9a in the Supporting Information.

To qualitatively assess the covalent attachment of the functional groups, ^{13}C cross-polarized magic angle spinning nuclear magnetic resonance (CP MAS NMR) was used, and the comparison of the chemical shift of carbon six (C6) of the functional groups before and after the reaction was carried out; the spectra displayed in Figure S9b, exhibit typical signals of cellulose at 107 (C1), 76 and 72 (C2, C3, and C5), and 66.6 and 64.4 ppm (C6). A parallel of this data with the spectra of phosphate-MFC showed that the chemical shift of C6 shifts from 66.5 to 55.2 ppm after its substitution with a phosphate group. Instead, the methylated membranes have resonance lined at 105, 87/75, and 60 ppm.

X-ray diffraction (XRD) spectra of all three-hybrid membranes are shown in Figure S10. These were recorded in dry and wet conditions to identify the fluctuation in the interlayer spacing after the grafting of functional groups. A significant shifting of the 002 peak (d spacing) of phosphate (+5.7 Å) and methyl (+3.2 Å) compared to the pristine-MFC was recorded in dry conditions, which confirmed the wider interlayer spacing of phosphate grafted hybrid membranes and the following pattern: phosphate-MFC > methyl-MFC > pristine-MFC.[46,47] Instead, in wet conditions, a significant shrinking of the 002 peak (d spacing) (−2.1 Å) of methyl-MFC hybrid membranes (Figure S10, inlet), a wide interlayer spacing of pristine-MFC (+6.4 Å), and intermediate for phosphate-MFC (+1.3 Å) were recorded (Figure S10, inlet). Such shifts indicate a swelling of the membranes in water. Indeed, a high swelling of pristine-MFC membranes corresponds to lower interlayer spacing, and after the grafting of phosphate groups, low swelling was detected.[3] A drastic quenching of the methyl-MFC interlayer spacing in wet state could be ascribed to the tendency of the methyl groups to escape from the water interface and reorganize the fibers in more hydrophobic core regions. Thus, the fibers association strongly depends on the distribution of the methyl moieties along the cellulose chains and is induced by the more populated methyl patches. The improved aggregation could be due to the interplay between the swelling of the more polar regions and the connections developed because of the hydrophobic association.[48]

Sieving Performance of Grafted Hybrid Membranes. We defined an approach where the sieving performance of the

https://doi.org/10.1021/acsapm.1c00105
ACS Appl. Polym. Mater. XXXX, XXX, XXX−XXX

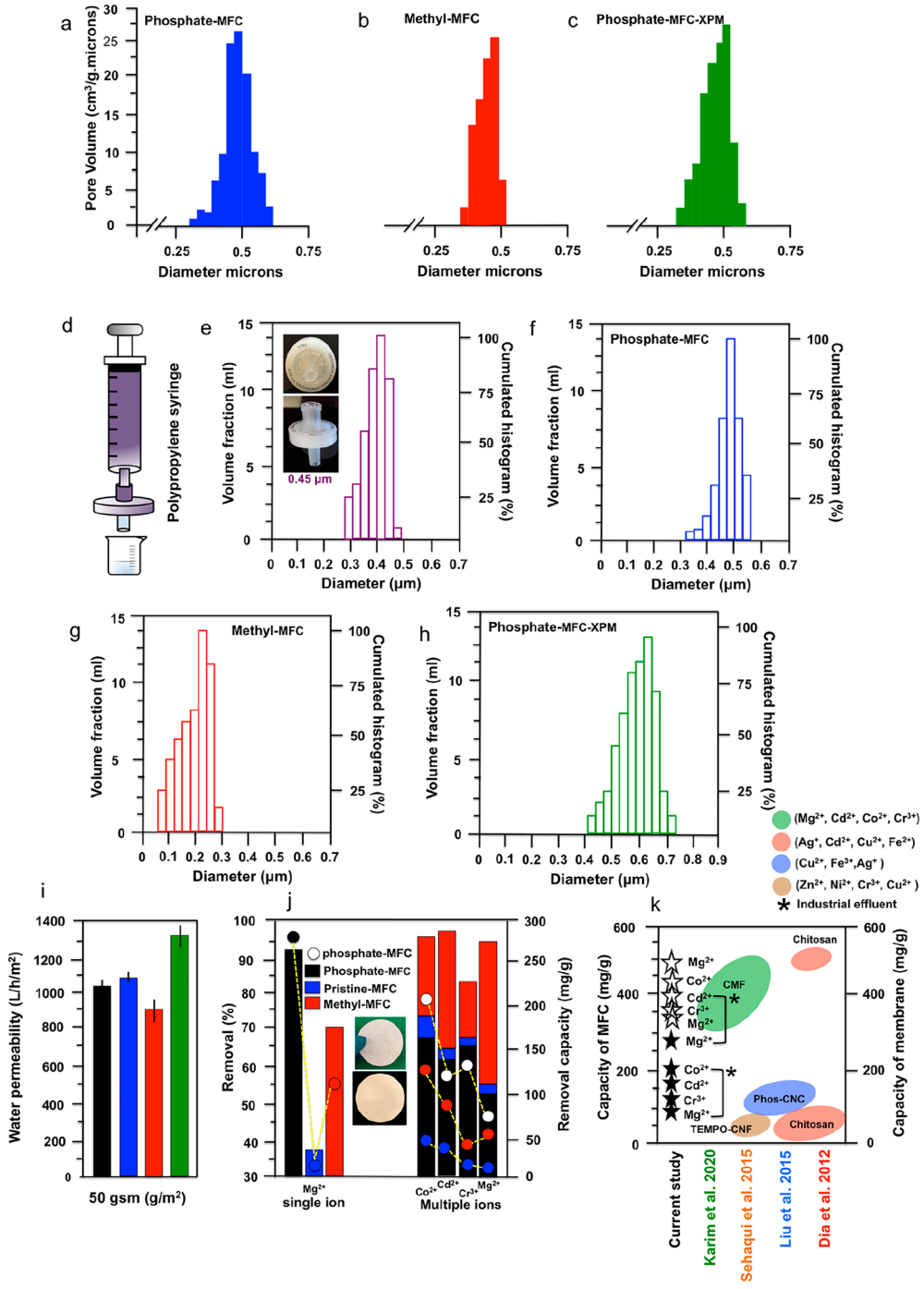

Figure 3. Pore structures and pore-size distribution of the fabricated laminated membranes using the BET analysis for (a) phosphate, (b) methyl, and (c) laminate membranes produced on XPM in continuous mode. (d and e) Particle size distribution of commercially available filter having a pore size of 0.45 μm using a simple filtration approach. A comparative study of the particle size distribution of the PEG nanoparticles via (f) phosphate-MFC, (g) methyl-MFC, and (h) membrane produced on XPM. (i) Water permeability of all four membranes (50 gsm) was analyzed; color coding: black, blue, red, and green are for pristine, lab scale phosphate-, methyl, and upscaled phosphate-composite membranes, respectively. (k) Adsorption of metal ions (water and industrial effluent model). (j) Comparative study with the literature.

fabricated composite membranes could be controlled by the grafted functional groups. The pore-size distribution of all hybrid membranes was measured using Brunauer−Emmett−Teller (BET) analysis (N_2 adsorption). A narrow pore-size distribution and low pore volume were detected for the pristine-MFC hybrid membrane (Figure S11a), where the mean pore size was approximately 0.27 μm. In parallel, a significant fluctuation in the pore-size distribution after grafting phosphate and methyl groups was observed, as displayed in Figure 3a,b. This fluctuation of the pores distributions is correlated with the type of the grafted functional groups, as evidenced by the theoretical predictions of an earlier investigation where it was found that the interlayer spacing of phosphate and methyl functionalizations was approximately 11.4 and 6.9 Å, respec-

https://doi.org/10.1021/acsapm.1c00105
ACS Appl. Polym. Mater. XXXX, XXX, XXX−XXX

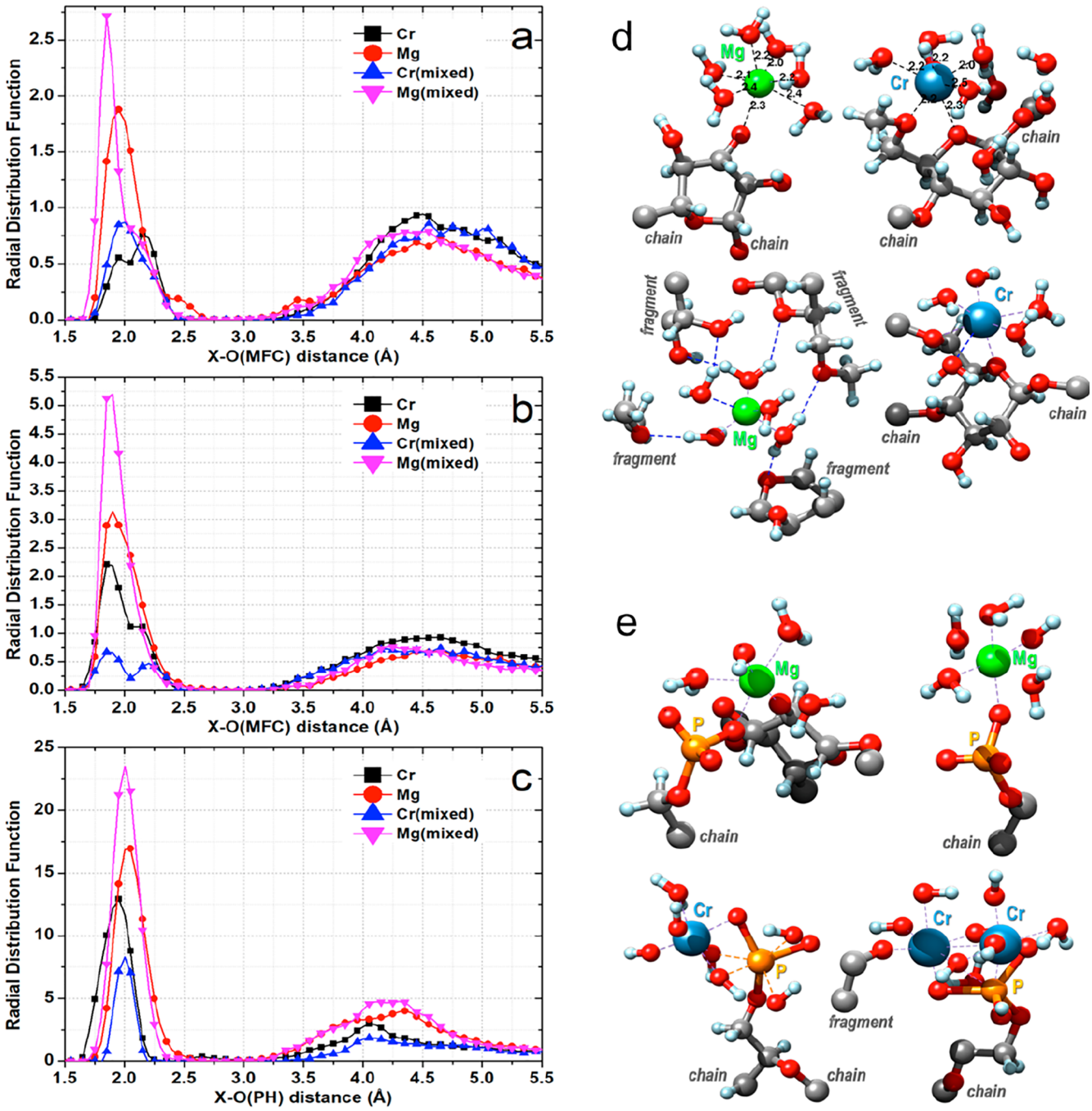

Figure 4. Atom−atom radial distribution functions describing the relative positions of the metal ions and the cellulose oxygens, namely, all cellulose chain oxygen, excluded the (a and b) phosphate head groups and (c) phosphate oxygens. (a) Methyl-MFC simulations and (b and c) phosphate-MFC simulations. The different metal ions concentrations are indicated in the legend: black = only Cr^{3+} ions; red = only Mg^{2+} ions; blu and magenta = 50% Mg^{2+} and 50% Cr^{3+} ions. Some of the possible binding modes of the Mg^{2+} and Cr^{3+} ions to the cellulose chains extracted from the final snapshot of the (d) methyl-MFC and (e) phosphate-MFC simulations.

tively.[3] A similar trend was observed in this work by using the N_2 adsorption analysis. It is worth mentioning that no significant change in pore-volume and -size distribution was detected in the upscaled hybrid membrane compared to its vacuum-filtered counterpart, which indicates that the up-scaling approach of hybrid membranes from the lab-to-pilot scale in water-based sustainable systems was accurate and balanced.

To further elucidate these mechanisms, we compared the sieving performance of the new membranes with that of commercially available filters having a pore diameter of 0.45 μm (Figure 3d,e), focusing on the filtration of polyethylene glycol (PEG) nanoparticles and the resulting particle size distribution after filtration (Figure 3f−h).

The PEG particle sizes from the commercial filters were distributed in a range of 0.25−0.55 μm (Figure 3e), whereas those obtained from the phosphate-MFC hybrid membranes (Figure 3f) explored a slightly larger range (0.30−0.61 μm) that well-compare with the data obtained from commercial devices. In parallel, a drastic decrease in the particle size distribution was recorded for the methyl-MFC hybrid membranes (Figure 3g),

https://doi.org/10.1021/acsapm.1c00105
ACS Appl. Polym. Mater. XXXX, XXX, XXX−XXX

confirming their more compact supramolecular organization with smaller openings. The PEG particles after filtration through the upscaled hybrid membranes (Figure 3h) were in a similar range as reported for vacuum-filtered hybrid membranes. These results suggest that tuning the interlayer spacing within the cellulosic hybrid membranes by grafting selected functional groups can significantly affect the membrane performance.

The effect of functional groups on the water permeance of active hybrid composite membranes was then investigated using the customized dead-end cell technique (Figure S4a). The density of fabricated hybrid membranes was adjusted to 50 g/m^2 by controlling the filtered hybrid volume. The water permeability of all composite membranes was tested with respect to operation time (Figure S12). A drastic decline of the water flow for the methyl-MFC composite membrane was obtained up to 120 min, and after that, a stable water flow was observed. In parallel, a shorter decline time was recorded for all other membranes compared to upscaled-MFC membranes. In the case of pristine-MFC hybrid membranes, the water permeance reached up to 1050 L/h/m^2 (Figure 3i), 42-fold higher than that of the pristine-MFC nanosheet.[22,49] We tested the water permeance of other hybrid membranes similarly, using pure water in dynamic mode. A significant increase in water permeance due to the phosphate groups (1500 L/h/m^2) was obtained, whereas in the case of methyl groups, a decrease in the water flux was observed (900 L/h/m^2) (Figure 3i). This agrees with the close-to-ideal stacking of the grafted functional group networks, where the interfiber spacing is regulated by the *effective* size of the head groups and their electrostatic interactions with the neighboring species. The size of grafted functional groups decreases in the order of phosphates, and methyls, hydroxyls (in agreement with the computational studies), and a similar pattern was followed by the water permeation analysis. Interestingly, the water flux decreased with the polarity of functional groups, demonstrating the importance of controlling the surface chemistry of these hybrid systems[50−52] to enhance the water permeance across the membranes (Figure 3i).

To further validate the performance of our active membranes, we checked the behavior of the functionalization during microfiltration. We measured the performance rate of several metal ions in a dead-end configuration (Figure S4a). We selected model wastewater contaminated with Mg^{2+} (single ion system) and a real industrial effluent (multi ions system). The highest percentage removal (94%) was recorded for the phosphate-MFC hybrid membranes followed by the methyl-MFC; the lowest percentage was obtained with the pristine-MFC membranes in the case of magnesium ion in a single ion solution (Figure 3j), but in parallel, the removal percentage of ions from the industrial effluent was in the order of $Co^{2+} > Cr^{3+} > Cd^{2+} > Mg^{2+}$ for the phosphate-MFC hybrid membrane. A similar pattern was followed for methyl- and pristine-MFC composite membranes as detected by using ICP-OES. The ionic radii of Cd^{2+}, Co^{2+}, Mg^{2+}, and Cr^{3+} were 0.95, 0.88, 0.86, and 0.75 Å, respectively,[3,53] and the pore-size distribution of hybrid functionalized membranes were in the range 0.25−0.55 μm. Thus, the sieving of metal ions through the fabricated membranes was impossible. The surface charge densities of grafted functional groups were 120.4 ± 1.2, 8.6 ± 1.4, and 32.5 ± 2.3 μmol/g for phosphate-, methyl-, and pristine-MFC hybrid membranes, respectively (Table S1). All these data indicate that a higher concentration of negatively charged species maintained in the assemblages a greater adsorption capacity of the positively charged metal ions (strong electrostatic interactions).[21,54] It has been noted that methyl-MFC has a positive surface charge at acidic pH (5.0) (Figure 2b), which in principle should divert the binding of the positively charged metal ions. Instead, as demonstrated in the literature, chitin nanocrystals from crab shells with a positively charged surface can be efficiently used for the immobilization of negatively charged metal ions through a chelation binding mechanism.[55,56] This could explain our results, and we could speculate that a sort of trapping takes place also in the case of methyl groups, as shown by the simulation results in Figure 4a.

The highest removal (94%) of Mg^{2+} ions was obtained with the phosphate-MFC action for the single type of metal system compared to methyl-MFC (69%), whereas when different types of metal ions were present, a similar pattern of adsorption is being analyzed. We could speculate that the initial low concentration of magnesium ions (2000 μg/L) determined the high rate of removal in the single type of ions system. Saito and Isogai[57] reported that the primary factor influencing the adsorption selectivity of metal ions is their electronegativity. The electronegativity of the metal ions was in the order of $Cd^{2+} > Co^{2+} > Mg^{2+} > Cr^{3+}$,[58] which does not follow the separation order in the multiple ions system. The thermodynamics explanation of this sorption affinity we have observed is extremely challenging and requires long dedicated studies.

The hybrid functionalized membranes demonstrated remarkable performance toward water purification and metal ions capture compared to the current state-of-the-art (Figure 3k); the highest capacity (mg/g) of phosphate-MFC hybrid membranes was recorded for magnesium ions in a single type of ions system (500 mg/g); furthermore, approximately 300 mg/g was observed in industrial effluent (Figure 3k). Our results suggest that the packing of fibers has a direct influence on the resulted interlayer spacing and can be modulated appropriately to design more selective scavengers.

Characterization of the Binding Modes of the Ions and Their Self-Interactions. The analysis of the simulation results that identified the capture mechanisms in the two cellulose models was mainly based on the inspection of the RDFs and visualization of the regions surrounding all the ions, separately.

The starting configurations were prepared in such a way that all the ions were well-solvated, located far apart from each other, and positioned relatively far from the cellulose supports. Still, already during the equilibration period, the ions started to approach the cellulose interface and to interact with the various oxygens of the chains directly or through the mediating action of the water molecules of the first solvation shell. In fact, when not in contact with the cellulose chains, the two metal ions appeared as hexa-aqua-metal ions ($[Cr(H_2O)_6]^{3+}$, $[Mg(H_2O)_6]^{2+}$), octahedrally coordinated by six water molecules.

The high affinity of these ions for the oxygen atoms resulted in a relatively strong water-metal electrostatic association that was responsible for three possible types of connections of the other species close by. The experimental data are also suggesting that the electrostatic interactions are the dominant mechanism for the separation of the metal ions. The binding reactions could involve the outer coordination sphere (binding with the interposed water molecules), the inner sphere (exchange reactions), or both of them, and the processes could compete with each other, influencing the rate of the whole mechanisms.

The extent of the local water content and the arrangement of the cellulose chains were the main features that regulated the ions binding mode, and the propensity to interact through the

https://doi.org/10.1021/acsapm.1c00105
ACS Appl. Polym. Mater. XXXX, XXX, XXX−XXX

inner-sphere increased with the local hydrophobicity. In the case of phosphates, it was found that, besides outer-sphere interactions (mainly hydrogen bonds), monodentate, bidentate, and bridge bidentate inner-sphere complexes could be formed. This was mostly observed in the case of Mg^{2+}, whereas the chromium ion was often found as $[Cr(H_2O)_5OH]^{2+}$ species and not as $[Cr(H_2O)_6]^{3+}$. The whole scenario depicted by the simulations entirely agrees with the experimental/theoretical observations reported in the literature regarding the structure and behavior of Mg^{2+} and Cr^{3+} ions in solutions and their fundamental binding modes to different types of compounds.[59]

As the RDFs plots shown in Figure S13c,d suggest, the first solvation layer, identified by the sharp peaks at around 2.1 Å with a minimum at approximately 2.8 Å, is relatively stable and does not exchange solvent molecules with the second layer. This is confirmed by the flat region between the first and the second peaks at about 4.3 and 4.5 Å for the methyl-MFC and phosphate-MFC systems, respectively. Notwithstanding the common trend, it is apparent that the presence of phosphate moieties affected the shape of the first solvation layer, inducing a reduction of the peaks' heights and the splitting and shifting of the peaks to shorter (around 1.8 Å) and longer (2.25 Å) distances, both in pure and mixed solutions. These findings indicate a stronger attraction of the ions to the phosphate head groups and a preference for Mg^{2+}. The visualization of the various ion-capturing modes by the cellulose oxygens revealed different scenarios, including single connections, group cooperation effects (involving various nearby chains), indirect binding by intermediate water molecules, ions self-interactions, or mixed Cr−Mg binding, but in all cases. Peaks splitting/shifting effects are also visible in the RDFs plots of the ions with all the cellulose oxygens, phosphate excluded (Figure 4a,b and Figure S13c,d). A partial solvation shell was always present (Figure 4d,e and Figures S14 and S15). Similarly, the dominant, sharp Mg^{2+} peaks at short distances and the broader lower Cr^{3+} peaks in the same range in all the RDFs plots of Figure 4 and Figure S16 indicate, indeed, that, in all types of solutions, both Cr^{3+} and Mg^{2+} can be close to the phosphate head groups (1.95−2.05 Å). Then, the examination of the coordination number, which in the case of Mg was almost twice the value of Cr, revealed that the phosphate moieties could capture more Mg^{2+} than Cr^{3+} ions. The inspection of the mixed ion solutions also suggests that multiple types of ions influence their mutual adsorption due to competitive binding, and the ion-coordinated waters are perturbed in their number and configuration. In fact, some are replaced by the phosphate oxygens, while others remain connected to their ions, readapting their arrangement to the new environment.

In sum, the overall tendency of the ions was to be connected/adsorbed to the MFC matrixes while preserving a variable amount of coordinated solvent oxygens and interacting with each other. Indeed, a limited self-aggregation of the metal ions was observed in both the mixed and pure ion solutions, together with the formation of small mixed aggregates made of three ions at most. In the case of magnesium, we could identify a diatomic cluster where the two ions were at a distance of about 3.3 Å. This is not surprising because these species have been observed experimentally and predicted by quantum chemistry calculations.[60,61]

Characterization of the Porous Structure of the MFC Models Ion Location and Dynamics. To provide a picture of a possible organization of the MFC matrixes during water and ion adsorption, the final sampled structures were displayed, highlighting their channels and pockets (identified and characterized by means of the CAVER analyst software) in Figure S17 of the Supporting Information. There, the methyl-MFC and phosphate-MFC filters can be compared by considering pockets distribution and size (gray, orange/red regions shown as solid surfaces in the top figures of each model), water permeation (cyan stick in the central figures of each model), and channels size and location (empty white zones in the bottom figures of each model).

At first sight, it is evident that, in the phosphate-MFC model, the water flux is remarkable, and practically, the water molecules flow from one side to the other side of the box. The cellulose chains are more loosely arranged, the number and size of the pockets are larger than the corresponding descriptors of the methyl-MFC structure, and the total volume of the channels is 20% greater. Even though the water content of the two models is similar, the distribution inside the matrixes is quite different, showing high water content confined in the big channels on top of the methyl-MFC model and almost no waters in the bulk portion of the structure. This suggests that the tight packing of the glucosyl chains prevents a fast translocation of the solvent and of the ions too.

Further details on the location of the ions inside channels and pockets can be achieved by an inspection of two sections of the membranes shown in Figure 5 and Figures S18 and S19. Focusing on the ion position, it can be noticed that, in the methyl-MFC model (Figure 5c,d), the ions remain prevalently inside the water pockets, close to their walls, and only a few tend to migrate toward the tiny central channels driven by the movements of a few water molecules. No ions are found in the

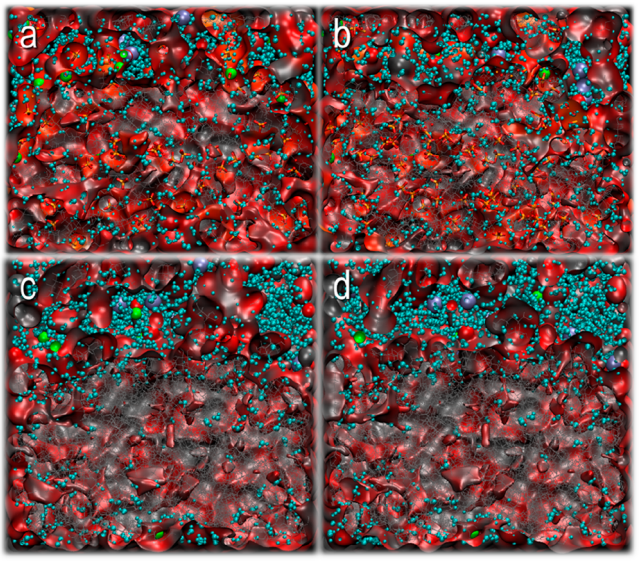

Figure 5. Snapshots extracted from the final stage of the MD simulations of the (a and b) hybrid phosphate-MFC and (c and d) methyl-MFC models in water solutions containing Mg^{2+} and Cr^{3+} ions. Each image represents a section of the simulation box where solid surfaces, rendered through gray and red regions representing the carbon/hydrogen and oxygen contributions, highlight the porous morphology of the cellulose matrix. Various pockets and tunnels containing water molecules (cyan spheres and $^{2+}$ and Cr^{3+} ions (green and ice-blue spheres, respectively) are visible. The cellulose chains are rendered through gray lines, orange, and sticks to highlight phosphate groups (a, b). For each simulation, two different box sections are displayed.

https://doi.org/10.1021/acsapm.1c00105
ACS Appl. Polym. Mater. XXXX, XXX, XXX−XXX

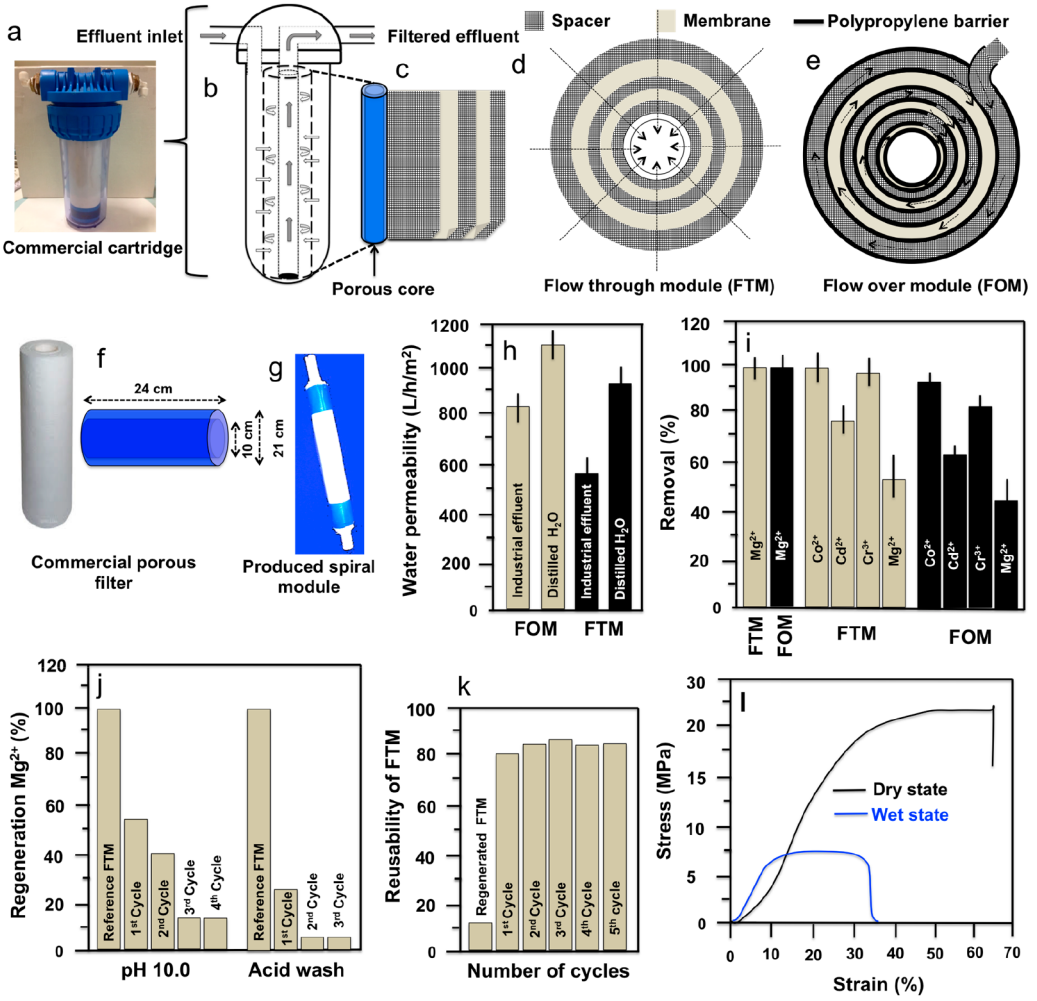

Figure 6. Module design and separation performance. (a) Commercially available cartridge. (b) Sketch represents the flow of water for separation of impurities. (c) Configuration arrangement of membranes for production of spiral wound modules. Two types of spiral wound modules, namely, (d) flow-through module and (e) flow-over module, were designed. (f) Commercial porous filter and (g) the produced filter are displayed. (h) Water permeability of FOM and FTM with distilled water and industrial effluent. (i) Separation of the metal ions through the modules. (j) Regeneration studies by changing in the pH (10.0) and acid wash were performed only for FTM. (k) Reusability of FTM. (l) Long-term stability of used laminated membrane was carried out in dry and wet conditions.

bulk portion of the matrix, which hosts only scattered water molecules. The situation is totally different when the chains are functionalized with phosphates. Water is concentrated in a few pockets but also distributed in the tunnels of the bulk; the ions can reach the central region of the matrix and remain entrapped there due to their strong interactions with the phosphate head groups that are randomly distributed along the cellulose chains.

Module Design and Performance Test at Pilot Scale. A very novel approach was adapted for the real test of hybrid membranes on an industrial scale. Only phosphate-MFC-based hybrid membranes were upscaled using the traditional paper-making approach (fully water-based sustainable system) on XPM in roll-to-roll[27] (Figure S1). The modules of phosphate-MFC hybrid membranes (Table S3) were designed for cartridge application (Figure 6a), and a diagrammatic representation is given in Figure 6b. Two modules, flow-through module (FTM) and flow-over module (FOM), were produced as mentioned in the Supporting Information (Figure S2), a spiral design was followed, as shown in Figure S2d,e, and the final spiral module is shown in Figure 6g and Figure S2f. Various porous cores used for the production of cartridge spiral modules are shown in Figure 6f and Figure S3 (with inner and outer diameters' range). It must be noted that modules were designed in such a way that maximum interactions of pollutants with available functional groups are possible. For FTM, water passed through the pores of hybrid membranes for maximum interactions between pollutants and grafted functional groups. (Figure 6d); in parallel, the flow of polluted water over the membranes is only possible in FOM (Figure 6e).

First, the water permeability of designed modules was measured using distilled water and industrial effluent, as shown in Figure S4b, in continuous mode. As expected, a high water permeability was calculated for the FOM, due to the free flow of water on the surface of used[62−64] (Figure 6h), indeed, by using both used waters (distilled and industrial water). The cross-flow system, as shown in Figure S4b, was also used for the separation of metal ions from polluted water, and all the applied parameters for the separation process are reported in Table S4. Our measurement revealed that the removal percentage ($R\% = C_{untreated} - C_{treated}/C_{treated} \times 100$) for single magnesium ions was 100. Moreover, a high removal was recorded by FTM compared to the FOM designed modules (Figure 6i). Notably, the

https://doi.org/10.1021/acsapm.1c00105
ACS Appl. Polym. Mater. XXXX, XXX, XXX−XXX

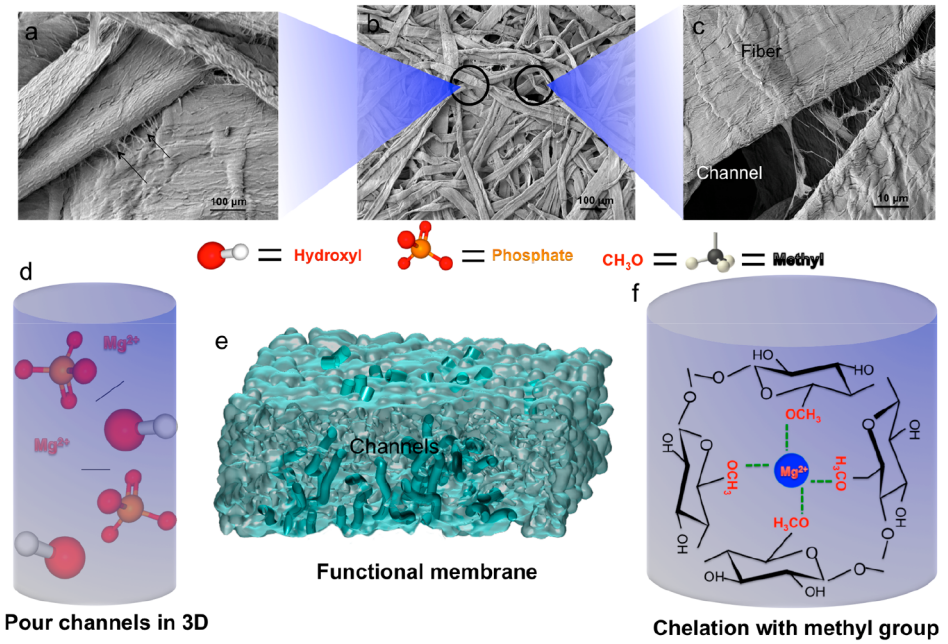

Figure 7. SEM images of upscaled active composite membranes showed (a) a connection with long pine fibers with MFC, (b) a low-resolution image of online produced active membranes, and (c) a high-resolution image of membranes with a pour channel. Diagrammatic 3D representations of (d) pour channels available within the produced active membranes, (e) interactions of metal ion (Mg^{2+}) with grafted phosphate functional groups with the pour channel, and (f) possible chelation mechanism for bindings of metal ions by methyl-MFC composite membranes.

complete removal of Co^{2+} and Cr^{3+} was recorded for FTM, but a low percentage removal (Co^{2+} = 90 and Cr^{3+} = 87) was calculated for FOM. The surface area available for the interactions of the ions is higher in FTM compared to FOM. Hence, the binding of ions with high densities of functional groups is possible in FTM.[22,65] Furthermore, a low initial concentration of metal ions has a direct influence on the high removal efficiencies of the modules[21,66−68] (Table S2). An energy dispersive spectroscopy (EDS) image of Mg ions adsorption on the membranes of FTM is given in Figure S20a, and the surface morphology of FTM membranes after the separation of metal ions from industrial effluent is shown in Figure S20b. Not any single fiber is visible after the filtration of industrial effluent.

Desorption and Reusability. The ability to desorb metal ions from an adsorbent is a crucial factor in determining the lifetime of the adsorbent. Thus, the regeneration of the used module was investigated. In the current study, fluctuation in pH and 1 M HCl was selected to study the regeneration (Figure 6j). The fluctuations in ζ-potential with respect to pH are shown in Figure 2b and indicate −5 mV at pH 10.0. The 7 L solution of pH 10.0 was prepared and passed through the module; 48% recovery of magnesium ions was calculated in the first cycle (Figure 6j). A significant regeneration of the module was calculated in the third cycle but no further detachment of ions was recorded in the fourth. In the second set of regeneration studies, 1 M HCl was used for the separation of magnesium ions; a regeneration value of approximately 70% was obtained in the first cycle, and a significant decrease in the second cycle was detected (Figure 6j). The results follow the same pattern reported in recent studies.[12,13,28] Furthermore, to check the reusability, a regenerated module was further applied for the separation of Mg ions. First, the module was washed with distilled water, and model water at pH 5.0 contaminated with ions was passed through the module in cross-flow mode. It is not surprising that 82% recovery was detected in the third passage of water, and no adsorption of ions was detected further (Figure 6k). The wet stability of membranes is shown in Figure 6l. A 4-fold decrease in tensile strength was recorded compared to that of dry membranes. Indeed, the breaking of the hydrogen bonds in water made the membranes less strong.[16] Instead, the adsorption capacity of the module remained unchanged, which suggests that the regeneration using a pH change and acid treatment was successful.

Evaluation of Nanochannels in Upscaled Composite Membranes. We were interested to disclose the reason for the high water permeability of the upscaled hybrid membranes compared to the vacuum-filtered ones. The alignment of the fibers during the upscaling of hybrid membranes was observed and further confirmed by the tensile strength and SEM analyses.[27] In the current work, we hypothesized that the increase in water passage is due to the existence of nanochannels (Figure 7) because of the alignment of the fibers toward the machine direction. To confirm this hypothesis, the SEM images of produced hybrid membranes were analyzed in detail (Figure 7a−c). A deep nanochannel between the fibers could be easily seen (Figure 7c). This allows for the free flow of water through the membranes. On the basis of the above findings, we propose to expand our viewpoint on the directed water channels, which are controlled by the gap between the aligned fibers.[8]

CONCLUSION

We have explained that the attachment of polar and nonpolar functional groups using chemo-enzymatic approaches can efficiently control the interlayer spacing and enhance the sieving performance of hybrid functional membranes. The hybrid functional membranes demonstrate remarkable performance toward water purification compared to the current state-of-the-art. We have succeeded in transferring technology from the lab to the pilot scale, and the upscaled hybrid membranes were

https://doi.org/10.1021/acsapm.1c00105
ACS Appl. Polym. Mater. XXXX, XXX, XXX−XXX

further used for the production of cartridge modules. Two modules (i.e., FTM and FOM) were designed according to the flow of water and applied for the removal of metal ions from industrial effluent. Our results suggest that polluted water passing through the pore of membranes is effectively purified. Furthermore, regeneration and reusability studies suggested the breakthrough in purification using modules. We believe that our strategy paves the way for the preparation of hybrid membranes with high functional groups and tunable sieving behaviors. The control of the surface chemistry of 2D hybrid membranes allows for the further exploitation of the nanofluidic phenomenon inside hybrid membranes at fundamental and practical levels for water purification. Furthermore, the produced modules have outstanding capabilities and are now ready for a real field test. Changes in the structural morphology from 2D to sphere could also be achieved in the future for the replacement of the packed bed column (Figure S21).

■ ASSOCIATED CONTENT

Supporting Information

The Supporting Information is available free of charge at https://pubs.acs.org/doi/10.1021/acsapm.1c00105.

Discussions of functionalization of MFC, characterization of 2D laminated functional membranes, metal ions removal experiments, and molecular dynamics simulations, tables of physical properties of produced functional membrane, concentration of metal ions in industrial effluent, properties of upscaled phosphate membrane used for modules design, and comparison of dynamic performance between FTM and FOM modules, and figures of Experimental Paper Machine schematic, designed and produced modules images, cartridge images, filtration and purification schemes, thermalized structure of the hybrid MFC and fiber models, XPS spectra, CP MAS NMR spectra, XRD spectra, BET analysis, water permeability, metal ions radial distribution functions, snapshots extracted from the final stage of the MD simulations, and EDS and SEM images (PDF)

■ AUTHOR INFORMATION

Corresponding Authors

Zoheb Karim − *MoRe Research Örnsköldsvik AB, SE-89122 Örnsköldsvik, Sweden;* orcid.org/0000-0002-4196-8419; Phone: +46 764221267; Email: zoheb.karim@gmail.com; Fax: +46 66075981

Susanna Monti − *CNR-ICCOM, Institute of Chemistry of Organometallic Compounds, I-56124 Pisa, Italy;* orcid.org/0000-0002-3419-7118; Email: sapetides@gmail.com

Complete contact information is available at: https://pubs.acs.org/10.1021/acsapm.1c00105

Notes

The authors declare no competing financial interest.

■ ACKNOWLEDGMENTS

Prof. Kang Li (Imperial College London) is highly acknowledged for helping in module design. The authors are also thankful to Prof. Aji P Mathew (Stockholm University, Sweden) for a detailed discussion. Computational support from the CINECA supercomputing center within the ISCRA program is gratefully acknowledged.

■ REFERENCES

(1) Shannon, M. A.; Bohn, P. W.; Elimelech, M.; Georgiadis, J. G.; Marinas, B. J.; Mayes, A. M. Science and technology for water purification in the coming decades. *Nature* **2008**, *452*, 301−310.

(2) Hussein, A. K. Applications of nanotechnology in renewable energies: A comprehensive overview and understanding. *Renewable Sustainable Energy Rev.* **2015**, *42*, 460−476.

(3) Karim, Z.; Monti, S.; Barcaro, G.; Svedberg, A.; Ansari, M. A.; Afrin, S. Enhanced sieving of cellulosic microfibers membranes via tuning of interlayer spacing. *Environ. Sci.: Nano* **2020**, *7*, 2941−2952.

(4) Qu, X.; Brame, J.; Li, Q.; Alvarez, P. J. J. Nanotechnology for a safe and sustainable water supply: enabling integrated water treatment and reuse. *Acc. Chem. Res.* **2013**, *46*, 834−843.

(5) Sholl, D. S.; Lively, R. P. Seven chemical separations to change the world. *Nature* **2016**, *532*, 435−437.

(6) Warsinger, D.; Chakraborty, S.; Tow, E. W.; Plumlee, M. H.; Bellona, C.; Loutatidou, S.; Karimi, L.; Mikelonis, A. M.; Achilli, A.; Ghassemi, A.; et al. A review of polymeric membranes and processes for potable water reuse. *Prog. Polym. Sci.* **2018**, *81*, 209−237.

(7) Guillen, G. R.; Pan, Y.; Li, M.; Hoek, E. M. V. Preparation and characterization of membranes formed by nonsolvent induced phase separation: A review. *Ind. Eng. Chem. Res.* **2011**, *50*, 3798−3817.

(8) Quellmalz, A.; Mihranyan, A. Citric acid cross-linked nanocellulose based paper for size-exclusion nanofiltration. *ACS Biomater. Sci. Eng.* **2015**, *1*, 271−276.

(9) Logan, B. E.; Elimelech, M. Membranes based processes for sustainable power generation using water. *Nature* **2012**, *488*, 313−319.

(10) Ma, H.; Burger, C.; Hsiao, B. S.; Chu, B. Ultrafiltration polysaccharide nanofibrous membranes for water purification. *Biomacromolecules* **2011**, *12*, 970−976.

(11) Yuan, J.; Liu, X.; Akbulut, O.; Hu, J.; Suib, S. L.; Kong, J.; Stellacci, F. Superwetting nanowire membranes for selective absorption. *Nat. Nanotechnol.* **2008**, *3*, 332−336.

(12) Ma, H.; Burger, C.; Hsiao, B. S.; Chu, B. Nanofibrous microfiltration membranes based on cellulose nanowhiskers. *Biomacromolecules* **2012**, *13*, 180−186.

(13) Ma, H.; Hsiao, B. S.; Chu, B. Ultrafine cellulose nanofibers as efficient adsorbents for removal of UO_2^{2+} in water. *ACS Macro Lett.* **2012**, *1*, 213−216.

(14) Zhu, Q.; Pan, Q. Mussel-inspired direct immobilization of nanoparticles and application for oil-water separation. *ACS Nano* **2014**, *8*, 1402−1409.

(15) Goetz, L. A.; Jalvo, B.; Rosal, R.; Mathew, A. P. Superhydrophilic anti-fouling electrospun cellulose acetate membranes coated with chitin nanocrystals for water filtration. *J. Membr. Sci.* **2016**, *510*, 238−248.

(16) Zhu, C.; Monti, S.; Mathew, A. P. Nanofiber−Graphene Oxide biohybrids: disclosing the self-assembly and copper-ion adsorption using advanced microscopy and ReaxFF simulations. *ACS Nano* **2018**, *12*, 7028−7038.

(17) Valencia, L.; Monti, S.; Kumar, S.; Zhu, C.; Liu, P.; Yu, S.; Mathew, A. P. Nanocellulose/graphene oxide layered membranes: elucidating their behaviour during filtration of water and metal ions in real time. *Nanoscale* **2019**, *11*, 22413−22422.

(18) Valencia, L.; Nomena, E. M.; Monti, S.; Rosas-Arbelaez, W.; Mathew, A. P.; Kumar, S.; Velikov, K. P. Multivalent ion-induced re-entrant transition of carboxylated cellulose nanofibrils and its influence on nanomaterials' properties. *Nanoscale* **2020**, *12*, 15652−1566.

(19) Zhu, H.; Luo, W.; Ciesielski, P. N.; Fang, Z.; Zhu, J. Y.; Henriksson, G.; Himmel, M. E.; Hu, L. Wood-derived materials for green electronics, biological devices, and energy applications. *Chem. Rev.* **2016**, *116*, 9305−9374.

(20) Hokkanen, S.; Bhatnagar, A.; Sillanpää, M. A. Review on modification methods to cellulose-based adsorbents to improve adsorption capacity. *Water Res.* **2016**, *91*, 156−173.

(21) Karim, Z.; Mathew, A. P.; Grahn, M.; Mouzon, J.; Oksman, K. Nanoporous membranes with cellulose nanocrystals as functional entity in chitosan: Removal of dyes from water. *Carbohydr. Polym.* **2014**, *112*, 668−676.

https://doi.org/10.1021/acsapm.1c00105
ACS Appl. Polym. Mater. XXXX, XXX, XXX−XXX

(22) Karim, Z.; Claudpierre, S.; Grahn, M.; Oksman, K.; Mathew, A. P. Nanocellulose based functional membranes for water cleaning: Tailoring of mechanical properties, porosity and metal ion capture. *J. Membr. Sci.* **2016**, *514*, 418−428.
(23) Kontturi, E.; Laaksonen, P.; Linder, M. B.; Gröschel, A. H.; Rojas, O. J.; Ikkala, O. Advanced materials through assembly of nanocelluloses. *Adv. Mater.* **2018**, *30*, 1703779.
(24) Sehaqui, H.; de-Larraya, U. P.; Liu, P.; Pfenninger, N.; Mathew, A. P.; Zimmermann, T.; Tingaut, P. Enhancing adsorption of heavy metal ions onto biobased nanofibers from waste pulp residues for application in wastewater treatment. *Cellulose* **2014**, *21*, 2831−2844.
(25) Valencia, L.; Kumar, S.; Jalvo, B.; Mautner, A.; Salazar-Alvarez, G.; Mathew, A. P. Fully bio-based zwitterionic membranes with superior antifouling and antibacterial properties prepared via surface-initiated free-radical polymerization of poly(cysteine methacrylate). *J. Mater. Chem. A* **2018**, *6*, 16361−16370.
(26) Dai, Y.; Sun, Q.; Wang, W.; Lu, L.; Liu, M.; Li, J.; Yang, S.; Sun, Y.; Zhang, K.; Xu, J.; Zheng, W.; Hu, Z.; Yang, Y.; Gao, Y.; Chen, Y.; Zhang, X.; Gao, F.; Zhang, Y. Utilizations of agricultural waste as adsorbent for the removal of contaminants: a review. *Chemosphere* **2018**, *211*, 235−253.
(27) Karim, Z.; Svedberg, A. Controlled retention and drainage of microfibrillated cellulose in continuous paper production. *New J. Chem.* **2020**, *44*, 13796−13806.
(28) Karim, Z.; Svedberg, A.; Lee, K. Y.; Khan, M. J. Processing-structure-property correlation understanding of microfibrillated cellulose based dimensional structures for ferric ions removal. *Sci. Rep.* **2019**, *9*, 10277.
(29) Montero, C.; Clair, B.; Almeras, T.; Lee, A. V. D.; Gril, J. Relationships between wood elastic strain under bending and cellulose crystal strain. *Compos. Sci. Technol.* **2012**, *72*, 175−181.
(30) Bolisetty, A. S.; Peydayesh, A. M.; Mezzenga, R. Sustainable technolofies for water purification from heavy metals: review and analysis. *Chem. Soc. Rev.* **2019**, *48*, 463−487.
(31) Xu, P.; Drewes, J. E.; Kim, T. U.; Bellona, C.; Amy, G. Effect of membranes fouling in transport of organic contaminants in NF/RO membranes applications. *J. Membr. Sci.* **2006**, *279*, 165−175.
(32) Kian, L. K.; Jawaid, M.; Ariffin, H.; Karim, Z. Isolation and characterization of nanocrustalline cellulose from roselle-derived microcrystalline cellulose, Int. *Int. J. Biol. Macromol.* **2018**, *114*, 54−63.
(33) Castro, D. O.; Karim, Z.; Medina, L.; Håggström, J. O.; Carosio, F.; Svedberg, A.; Wågberg, L.; Söderberg, D.; Berglund, L. A. The use of a pilot scale continuous paper process for fire retardant cellulose-kaolinite nanocomposites. *Compos. Sci. Technol.* **2018**, *162*, 215−224.
(34) Mair, M. *Control of porous structure of paper in a continuous process.* Master thesis, KTH Royal Institute of Technology, Stockholm, Sweden, 2016.
(35) Ankerfors, M.; Lindström, T.; Söderberg, D. The use of microfibrillated cellulose in fine paper manufacturing-Results from the pilot scale papermaking trial. *Nord. Pulp Pap. Res. J.* **2014**, *29*, 476.
(36) Zhu, C.; Monti, S.; Mathew, A. P. Evaluation of nanocellulose interactions with water pollutants using nanocellulose colloidal probes and molecular dynamic simulations. *Carbohydr. Polym.* **2020**, *229*, 115510.
(37) Carpenter, A. W.; de Lannoy, C. F.; Wiesner, M. R. Cellulose nanomaterials in water treatment technologies. *Environ. Sci. Technol.* **2015**, *49*, 5277−5287.
(38) Marczewski, A. W. Application of mixed order rate equations to adsorption of methylene blue on mesoporous carbons. *Appl. Surf. Sci.* **2010**, *256*, 5145−5152.
(39) Awual, M. R.; Hasan, M. M.; Iqbal, J.; Islam, M. A.; Islam, A.; Khandaker, S.; Asiri, A. M.; Rahman, M. M. Ligand based sustainable composite material for sensitive nickel(II) capturing in aqueous media. *J. Environ. Chem. Eng.* **2020**, *8*, 103591.
(40) Bozic, M.; Liu, P.; Mathew, A. P.; Kokol, V. Enzymatic phosphorylation of cellulose nanofibers to new highly-ions adsorbing, flame-retardant and hydroxyapatite-growth induced natural nanoparticles. *Cellulose* **2014**, *21*, 2713−2726.
(41) Chatterjee, T.; Nakatani, A. I.; Adden, R.; Brackhagen, M.; Redwine, D.; Shen, H.; Li, Y.; Wilson, T.; Sammler, R. L. Structure and properties of aqueous methylcellulose gels by small-angle neutron scattering. *Biomacromolecules* **2012**, *13*, 3355−3369.
(42) Kim, M. H.; Park, H.; Nam, H. C.; Park, S. R.; Jung, J.-Y.; Park, W. H. Injectable methylcellulose hydrogel containing silver oxide nanoparticles for burn wound healing. *Carbohydr. Polym.* **2018**, *181*, 579−586.
(43) Liu, P.; Borrell, P. F.; Božič, M.; Kokol, V.; Oksman, K.; Mathew, A. P. Nanocellulose and their phosphorylated. derivatives for selective adsorption of Ag^{+}, Cu^{2+} and Fe^{3+} from industrial effluents. *J. Hazard. Mater.* **2015**, *294*, 177−185.
(44) Voisin, H.; Bergström, L.; Liu, P.; Mathew, A. P. Nanocellulose-based materials for water purification. *Nanomaterials* **2017**, *7*, 57.
(45) Bourbigot, S.; Le Bras, M.; Gengembre, L.; Delobel, R. XPS study of an intumescent coating application to the ammonium polyphosphate/pentaerythritol fire-retardant system. *Appl. Surf. Sci.* **1994**, *81*, 299−307.
(46) Ries, L.; Petit, E.; Michel, T.; Diogo, C. C.; Gervais, C.; Salameh, C.; Bechelany, M.; Balme, S.; Miele, P.; Onofrio, N.; Voiry, D. Enhanced sieving from exfoliated MoS2 membranes via covalent functionalization. *Nat. Mater.* **2019**, *18*, 1112−1117.
(47) Hoga, H.; Nogi, M.; Komoda, N.; Nge, T. T.; Sugahara, T.; Suganuma, K. Uniformly connected conductive networks on cellulose nanofiber paper for transparent paper electronics. *NPG Asia Mater.* **2014**, *6*, e93.
(48) Lindman, B.; Medronho, B.; Alves, L.; Costa, C.; Edlund, H.; Norgren, M. Norgren The relevance of structure features of cellulose and its interections to dissolution, regeneration, gelation and plasticization phenomena. *Phys. Chem. Chem. Phys.* **2017**, *19*, 23704−23718.
(49) Daochalermwong, A.; Chanka, N.; Songsrirote, K.; Dittanet, P.; Niamnuy, C.; Seubsai, A. Removal of heavy metal ions using modified celluloses prepared from pineapple leaf fiber. *ACS Omega* **2020**, *5*, 5285−5296.
(50) Phillip, W. A.; Dorin, R. M.; Werner, J.; Hoek, E. M. V.; Wiesner, U.; Elimelech, M. Tuning structure and properties of graded triblock terpolymer-based mesoporous and hybrid films. *Nano Lett.* **2011**, *11*, 2892−2900.
(51) Govind-Rajan, A.; Sresht, V.; Pádua, A. A. H.; Strano, M. S.; Blankschtein, D. Dominance of dispersion interactions and entropy over electrostatics in determining the wettability and friction of two-dimensional MoS_2 surfaces. *ACS Nano* **2016**, *10*, 9145−9155.
(52) Wang, Z.; von-dem-Bussche, A.; Qiu, Y.; Valentin, T. M.; Gion, K.; Kane, A. B.; Hurt, R. H. Chemical dissolution pathways of MoS_2 nanosheets in biological and environmental media. *Environ. Sci. Technol.* **2016**, *50*, 7208−7217.
(53) Abraham, J.; Vasu, K. S.; Williams, C. D.; Gopinadhan, K.; Su, Y.; Cherian, C. T.; Dix, J.; Prestat, E.; Haigh, S. J.; Grigorieva, I. V.; Carbone, P.; Geim, A. K.; Nair, R. R. Tunable sieving of ions using graphene oxide membranes. *Nat. Nanotechnol.* **2017**, *12*, 546−550.
(54) Rathee, V. S.; Sidky, H.; Sikora, B. J.; Whitmer, J. K. Role of associative charging in the entropy−energy balance of polyelectrolyte complexes. *J. Am. Chem. Soc.* **2018**, *140*, 15319−15328.
(55) Han, Y.; Xu, C.; Gao, Z. Ultrathin grapheme nanofiltration membranes for water purification. *Adv. Funct. Mater.* **2013**, *23*, 3693−3700.
(56) Li, Z.; Yang, X.; Li, W.; Liu, H. Stimuli-responsive cellulose paper materials. *Carbohydr. Polym.* **2019**, *210*, 350−363.
(57) Saito, T.; Isogai, A. Ion-exchange behavior of carboxylate groups in fibrous cellulose oxidized by the TEMPO-mediated system. *Carbohydr. Polym.* **2005**, *61*, 183−190.
(58) Volesky, B. Biosorption and me. *Water Res.* **2007**, *41*, 4017−4029.
(59) *The Chemistry of Organomagnesium Compounds*; Rappoport, Z., Marek, I., Eds.; John Wiley & Sons, Ltd., 2008.
(60) Perera, L.; Beard, W. A.; Pedersen, L. G.; Wilson, S. H. Hiding in planin sight: The bimetallic magnesium covalent bond in enzyme active sites. *Inorg. Chem.* **2017**, *56*, 313−320.

https://doi.org/10.1021/acsapm.1c00105
ACS Appl. Polym. Mater. XXXX, XXX, XXX−XXX

(61) Aktulga, H. M.; Fogarty, J. C.; Pandit, S. A.; Grama, A. Y. Parallel reactive molecular dynamics: Numerical methods and algorithmic techniques. *Parallel Computing* **2012**, *38*, 245−259.
(62) Zhang, J.; Li, Z.; Zhan, K.; Sun, R.; Sheng, Z.; Wang, M.; Wang, S.; Hou, X. Two dimensional nanomaterialbased separation membranes. *Electrophoresis* **2019**, *40*, 2029−2040.
(63) Deng, M.; Kwac, K.; Li, M.; Jung, Y.; Park, H. G. Stability, molecular sieving, and ion diffusion selectivity of a lamellar membrane from two-dimensional molybdenum disulfide. *Nano Lett.* **2017**, *17*, 2342−2348.
(64) Zheng, S.; Tu, Q.; Urban, J. J.; Li, S.; Mi, B. Swelling of Graphene Oxide Membranes in Aqueous Solution: Characterization of Interlayer Spacing and Insight into Water Transport Mechanisms. *ACS Nano* **2017**, *11*, 6440−6450.
(65) Furukawa, H.; Gandara, F.; Zhang, Y. B.; Jiang, J.; Queen, W. L.; Hudson, M. R.; Yaghi, O. M. Water adsorption in porous metal-organic frameworks and related materials. *J. Am. Chem. Soc.* **2014**, *136*, 4369−4381.
(66) Zhang, Z.; Kang, G.; Yu, H.; Jin, Y.; Cao, Y. From reverse osmosis to nanofiltration: Precise control of the pore size and charge of polyamide membranes via interfacial polymerization. *Desalination* **2019**, *466*, 16−23.
(67) de-Grooth, J.; Oborny, R.; Potreck, J.; Nijmeijer, K.; de-Vos, W. M. The role of ionic strength and odd−even effects on the properties of polyelectrolyte multilayer nanofiltration membranes. *J. Membr. Sci.* **2015**, *475*, 311−319.
(68) Dickhout, J. M.; Kleijn, J. M.; Lammertink, R. G.; De-Vos, W. M. Adhesion of emulsified oil droplets to hydrophilic and hydrophobic surfaces−effect of surfactant charge, surfactant concentration and ionic strength. *Soft Matter* **2018**, *14*, 5452−5460.

https://doi.org/10.1021/acsapm.1c00105
ACS Appl. Polym. Mater. XXXX, XXX, XXX−XXX